ARTICLE OPEN

Check for updates

Full-color-tunable phosphorescence of antimony-doped lead halide single crystal

Jin-Feng Liao[1,2], Zhipeng Zhang[1,2], Bingzhe Wang[1], Zikang Tang[1]✉ and Guichuan Xing[1]✉

Although multiple emissive phosphors are of great fundamental interest and practical importance, it is still challenging to achieve full-color tunable luminescence in a single-component material. Herein, we present an antimony-doped lead halide single crystal $(C_{10}NH_{22})_2PbBr_4$: Sb^{3+} with widely tunable red/green/blue/white luminescence. Extrinsic Sb^{3+} dopants provide host another active sites to capture photo-generated excitons, thus triggering blue/red dual emission. Moreover, a reversible thermal-induced phase transition transforms blue/red emission into green/red dual emission. Both two phases exhibit intriguing excitation-wavelength dependent emission, affording a whole color gamut covering the red-green-blue (RGB) color triangle on the CIE 1931 diagram. Experimental and theoretical calculation studies reveal two emitters work independently, which paves the way for the multimode optical control and promotes the development of multifunctional luminescent materials.

npj Flexible Electronics (2022)6:57 ; https://doi.org/10.1038/s41528-022-00194-4

INTRODUCTION

During the past decade, the great renaissance of three-dimensional (3D) organic-inorganic lead halide materials has revolutionized the way of constructing high-performance optoelectronic devices[1–3]. According to the connection mode of metal halide polyhedrons, the great family of metal halides materials could be generally classified into 3D, 2D, 1D, and 0D structure, where polyhedrons connect with each other to form 3D network, 2D sheets, 1D chains, or completely isolate from each other. With reference to 3D structured metal halide, 2D, 1D and 0D metal halides are generally regarded as low dimensional metal halides materials. Along with the fruitful achievements in 3D metal halides, their low-dimensional counterparts have also received intense attention and recently become a research hot spot due to extraordinary self-trapped exciton (STE) emission properties (e.g., large Stokes shift and high luminescence efficiency)[4–7]. Compared with 3D metal halides, a larger degree of photo-induced structural distortion is favored in the excited state of lower structural dimension, which is conducive to the formation of STE[8–10]. Additionally, intense spatial confinement induced stronger exciton binding energy is beneficial for the radiative recombination of localized excitons, thus leading to high photoluminescence quantum yield (PLQY)[8,11–13]. With great efforts on the experimental and theoretical studies in recent years, a large number of low-dimensional luminescent metal halides have been developed with prominent emission efficiency. For instance, the foremost monometallic halide hybrid compounds of Sn^{2+}, Sb^{3+}, Pb^{2+}, Cu^{+} have known to exhibit bright STE emission with a PLQY up to near unity (e.g., $Cs_3Cu_2I_5$, $(DTA)_2SbCl_5$·DTAC and $(C_9NH_{20})_2SbCl_5$)[14–16]. Nevertheless, the STE emission of these monometallic compounds typically are monochromatic due to single-type inherent photoactive species[11,17]. Although blending micrometer-sized three-primary-color (red, green and blue) luminescent phosphors currently is most popular strategy to generate luminescence tunable materials with white light emission[18–20], re-absorption issues and varied decay rates between different phosphors adversely affect the luminescent efficiency and color stability[17,21]. Therefore, exploration of single-component multicolor luminescent materials is of significant importance but is still challenging[22].

Recently, doping/alloying of metal ions (e.g., Sb^{3+}, Sn^{2+}) has been reported as an effective strategy to endow metal halide materials with tunable dual emission due to the joint action of intrinsic and extrinsic emitter[23–25]. It is found that the luminescent properties of each light-emitting species could be well preserved in metal halides matrix without mutual interaction due to the space isolation[26,27]. However, despite recent success in dual emission, the design of wide-gamut color-tunable metal halide phosphor is still in infancy and largely unexplored[28–31]. To the best of our knowledge, tunable red/green/blue/white color emission has not been achieved in a single-phase metal halide material.

Herein, we have synthesized a antimony-doped lead halide single crystal, $(C_{10}NH_{22})_2PbBr_4$: Sb^{3+} with a tunable blue/red dual emission originating from the Pb^{2+}- and Sb^{3+}-associated STE relaxation. Interestingly, a reversible thermal-induced phase-transition of $(C_{10}NH_{22})_2PbBr_4$: Sb^{3+} could transform the blue/red dual emission into green/red dual emission due to transformed polyhedron configuration. Both the blue/red and green/red dual emission are sensitive to the excitation wavelength, which can manipulate the emission color gamut covering the RGB color triangle on the CIE 1931 diagram. As far as we know, the red/green/blue/white tunable emissive $(C_{10}NH_{22})_2PbBr_4$: Sb^{3+} is the widest color-range tunable luminescent metal halide, which is undoubtedly conducive to its practical applications as multi-purpose solid light emitter, temperature sensor and high-security anti-counterfeiting material.

RESULTS

Crystal sturcture of Pb-Br: Sb single crystal

Undoped and Sb^{3+}-doped $(C_{10}NH_{22})_2PbBr_4$ crystals were prepared by slowly diffusing diethyl ether vapor into the mother liquor at room temperature. Due to negligible visible light absorption, undoped $(C_{10}NH_{22})_2PbBr_4$ (denoted as Pb-Br) crystals are colorless and transparent under daylight (Fig. 1a). Introduction of Sb^{3+}

[1]Joint Key Laboratory of the Ministry of Education, Institute of Applied Physics and Materials Engineering, University of Macau, Avenida da Universidade, Taipa, Macau 999078, China. [2]These authors contributed equally: Jin-Feng Liao, Zhipeng Zhang. ✉email: zktang@um.edu.mo; gcxing@um.edu.mo

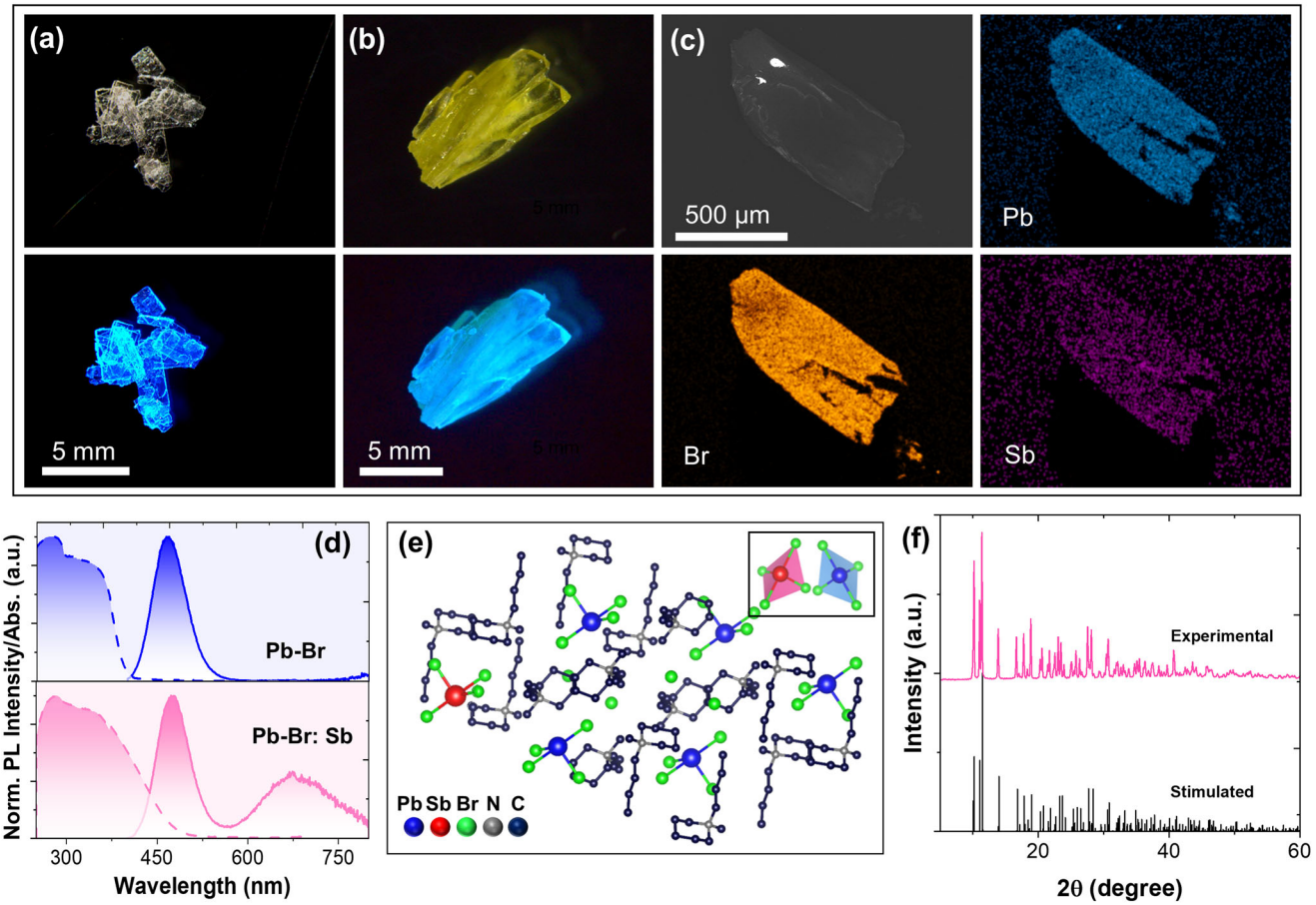

Fig. 1 Crystal structure and optical properties characterization. Optical images of Pb-Br (**a**) and Pb-Br: Sb (**b**) single crystals under daylight (top) and 365 nm UV light (bottom). **c** SEM image and elements mapping of Pb, Br and Sb in Pb-Br: Sb single crystal. **d** Normalized UV-vis absorption spectra (dotted line) and PL emission spectra (solid line) of Pb-Br and Pb-Br: Sb. **e** Schematic view of Pb-Br: Sb crystal structure, inset showing seesaw-shaped $PbBr_4^{2-}$ and $SbBr_4^-$ units. **f** Comparison of experimental and stimulated powder XRD patterns of Pb-Br: Sb.

results in additional absorbance in 400–500 nm region and renders crystal yellow body color under daylight (Fig. 1b, d). Rather than narrow-band blue emission in Pb-Br crystal, Sb^{3+}-doped crystals (denoted as Pb-Br: Sb) emit blueish-white light under excitation at 365 nm with intriguing dual-band emission. To gain more insight into the impact of extrinsic Sb^{3+} ions on photophysical properties of Pb-Br, the crystal structure was investigated. The isomorphous structure of Pb-Br and Pb-Br: Sb was consolidated by the single-crystal X-ray diffraction analysis, which reveals both two adopt a monoclinic space group of $C_{2/c}$ (Supplementary Table S1). Isolated seesaw-shaped tetrahedrons are completely surrounded by the organic cations ($C_{10}NH_{22}^+$), presenting a 0D organic-inorganic metal halide hybrid structure (Fig. 1e). Almost identical features were observed in the experimental and stimulated powder X-ray diffraction (PXRD) pattern, affirming the phase purity (Fig. 1f). X-ray photoelectron spectra (XPS) analysis showcases characteristic peaks of Sb 3d orbital at 532.02 eV and 539.18 eV in Pb-Br: Sb, which is corresponding to the binding energies of 3d5/2 and 3d3/2 of Sb^{3+} (Supplementary Fig. 1e and Supplementary Table 2)[27,32,33]. The binding energy of Pb 4 f and Br 3d in Pb-Br: Sb have been slightly shifted compared with Pb-Br, furthering verifying the successful of incorporating Sb^{3+} into the host matrix. The homogeneous distributions of Pb, Sb and Br in as-prepared single crystals were verified by the scanning electron microscope-energy dispersive X-ray spectrum elemental mapping (Fig. 1c). Furthermore, the impact of Sb^{3+} amount on the emission properties has been investigated. With the increase of Sb^{3+} content, the value of $I_{670\ nm}/I_{470\ nm}$ gradually increased (Fig. S2). However, other phase crystal was precipitated when the loading amount of $SbBr_3$ exceeds 5 mg (Fig. S3), which emits yellow-green PL emission with dual emission peaked at 545 and 725 nm. According to the SEM-EDS tests, the solubility limit of Sb^{3+} dopant in $(C_{10}NH_{22})_2PbBr_4$ is about 2%, and otherwise phase separation would appear, which is commonly seen in the non-equivalent doping process[27,32].

Optical studies of Pb-Br: Sb single crystal

In order to closely examine the dual-emissive origination of Pb-Br: Sb, monometallic Sb-based counterpart (denoted as Sb-Br) was synthesized as a reference (Supplementary Fig. 4). Regardless of the excitation wavelength, monometallic Pb-Br and Sb-Br exhibit monotonous emission peaking at 470 nm and 630 nm, respectively, originated from the triplet self-trapped excitons relaxing from ^3P_n to $^1S_0$ ($n = 0, 1, 2$) (Fig. 2a, S4 and S5)[16,34,35]. The onefold emission source of Pb-Br and Sb-Br could also be confirmed by their emission-wavelength dependent photoluminescence excitation (PLE) spectra, which showcase consistent features regardless of the emission wavelength (Supplementary Figs. 5 and 6). After incorporating Sb^{3+} into Pb-Br, high-energy emission band at 470 nm remains unchanged while extra PL and PLE band appear in low-energy region. The Sb^{3+}-associated emission is red-shifted in Pb-Br: Sb compared to monometallic Sb-Br, which can be assigned to the coordination environment changes. The formation of infrequent $SbBr_4^-$ in Pb-Br: Sb crystal lattice rather than familiar $SbBr_5^{2-}$ pyramid could be affirmed by the consistent maximum PL emission with previously reported seesaw-shaped $SnBr_4^{2-}$

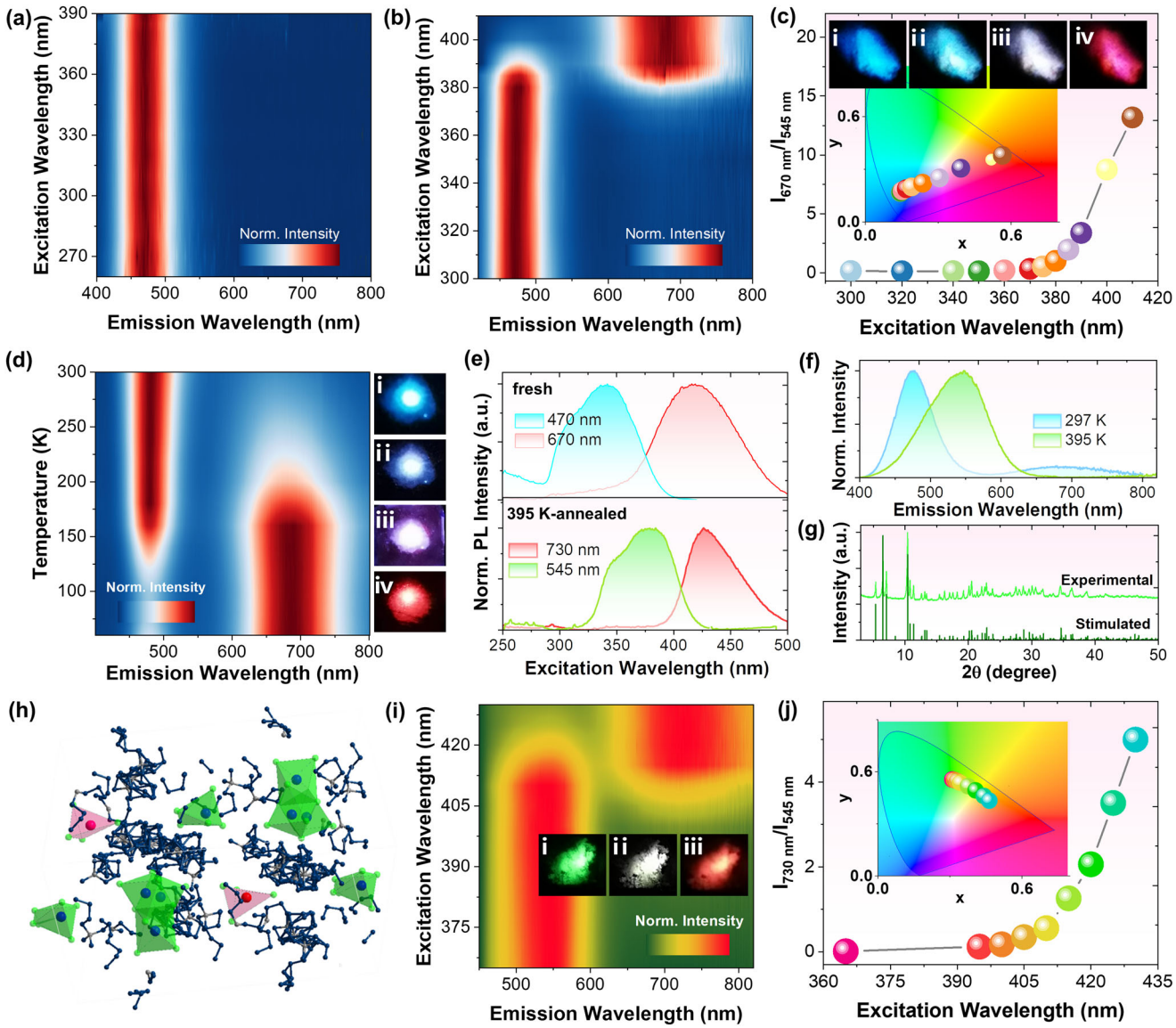

Fig. 2 Dynamic emission properties. Pseudo color map of excitation-wavelength-dependent PL emission of Pb-Br (**a**) and Pb-Br: Sb (**b**) at room temperature. **c** Excitation-wavelength-dependent ratio of $I_{670\ nm}$ to $I_{470\ nm}$ in Pb-Br: Sb. Inset shows the CIE coordinates for emission spectra in (**b**), and the optical images of Pb-Br: Sb power excited at (i) 360, (ii) 370, (iii) 380 and (iv) 400 nm. **d** Pseudo color map of temperature-dependent PL emission of Pb-Br: Sb, and the optical images of 365-nm-excited Pb-Br: Sb at (i) 300, (ii) 200, (iii) 180 and (iv) 80 K. **e** PLE spectra of Pb-Br: Sb at 300 K and 395 K. **f** Steady state PL emission spectra of 365-nm-excited Pb-Br: Sb at 300 K and 395 K. **g** Comparison of PXRD pattern of 395 K-annealed Pb-Br: Sb and the high-temperature phase of Pb-Br. **h** A schematic view of Sb^{3+}-doped $(C_{10}NH_{22})_9[Pb_3Br_{11}][PbBr_4]_2$ crystal structure. **i** Pseudo color map of excitation-wavelength-dependent PL emission of 395 K-annealed Pb-Br: Sb. Inset is the optical images of 395 K-annealed Pb-Br: Sb under excitation at (i) 360, (ii) 400 and (iv) 420 nm. (j) Excitation-wavelength-dependent CIE coordinates and emission intensity ratio of 730/545 nm in fresh 395-K-annealed Pb-Br: Sb.

(670 nm)[35,36]. It is found that the intensity ratio of dual emission band in Pb-Br: Sb is highly sensitive to the excitation wavelengths (Fig. 2b). As excitations shift to low energy UV light, red emission gradually builds up with the attenuation of blue emission, making $I_{670\ nm}/I_{470\ nm}$ value enlarging from 0.163 to 13.2 (Fig. 2c). The luminescent color variations in response to different excitations are plotted in the Commission International de l'Eclairage (CIE) coordinate diagram, and the detailed coordinates are summarized in Supplementary Table 3. As excitation shifts from 360 nm to 400 nm, the emission color changes from blue to red with a white light obtained under 380 nm excitation (Fig. 2c (i-iv)). The strictly linear relationship between excitation and CIE coordinates suggests that the dynamic tunable emission of Pb-Br: Sb is derived from a color complex without complex energy transfer. Systematic emission wavelength dependent excitation spectra measurements clearly demonstrate the dual emission in Pb-Br: Sb is originated from two different excited states (Supplementary Fig. 7). High-energy and low-energy emission bands have distinct PLE features peaking at 330 nm and 430 nm, respectively (top in Fig. 2e). Agreeing well with the UV-vis absorption spectra, $PbBr_4^{2-}$ are nearly inert to the low energy photons while Sb^{3+}-associated clusters are actively responsive, thus leading to bright red emission (Fig. 2c (iv)).

In addition to the intriguing excitation dependent behavior, the dual emission in Pb-Br: Sb shows a strong dependence on the temperature. The $I_{670\ nm}/I_{470\ nm}$ ratio decrease from 3.23 to 0.234 (Supplementary Fig. 8) as temperature gradually increases from 80 to 300 K, which endows 365-nm-excited Pb-Br: Sb with

temperature-dependent emission color (Fig. 2d (i-iv)), changing from red to pink, white and sky-blue. Similar phenomenon has been observed when switching to 380 nm UV light excitation. As temperature decreases, $I_{670\ nm}/I_{470\ nm}$ value increases from 1.13 to 20.1, which resulting the luminescence color of Pb-Br: Sb turning from white light into deep red (Supplementary Fig. 9). Subsequently, the emissive properties of Pb-Br: Sb above the room temperature have been further investigated. Sky-blue luminescence of 365-nm-excited Pb-Br: Sb was well maintained until temperature rises to 395 K. The green emission amazingly appears at 395 K with the PL maximum emission peak shifted to 545 nm from the original 470 nm (Fig. 2f and Supplementary Fig. 10). Similar phenomenon has been also found in undoped Pb-Br, which is originated from the thermal induced phase transition, as confirmed by the temperature-dependent XRD studies (Supplementary Fig. 11). Fresh 395-K-annealed Pb-Br: Sb showcases a distinct XRD pattern from the original Pb-Br but similar with its high-temperature phase, $(C_{10}NH_{22})_9[Pb_3Br_{11}][PbBr_4]_2$, which consists of isolated $[Pb_3Br_{11}]^{5-}$ trimer and $PbBr_4^{2-}$ tetrahedron (Fig. 2g and h)[37]. This result suggests a thermal-induced phase transition from Pb-Br: Sb (denoted as phase I) to Sb^{3+}-doped $(C_{10}NH_{22})_9[Pb_3Br_{11}][PbBr_4]_2$ (denoted as phase II) occurs upon annealing at 395 K. This conclusion can be further confirmed by the differential scanning calorimetry (DSC) and temperature-depenent XRD tests. As shown in the Supplementary Fig. 12, the DSC curve shows a peak around 103 °C, indicating a phase transition occurs consistent with the temperature dependnet XRD results. The XRD patterns were well maintained in the temperature range from −70 °C to 80 °C, suggesting that the temperature-dependent emission color change within this temperature range is due to the different temperature sensitivity between Pb^{2+} and Sb^{3+} associated STE (Supplementary Fig. 13). When increasing to 110 °C, some signals appeared at the low diffraction angle in the XRD pattern, suggesting the phase transformation occurs. The altered crystal structure further resulted in the emission color change. In addtion, the thermal stability was studied by the thermogravimetric analysis indicatng that the Sb^{3+} doped $(C_{10}NH_{22})_2PbBr_4$ has high thermal stability without decomposition at 200 °C (Supplementary Fig. 14). Interestingly, the phase transition has transformed the original blue/red dual emission into green/red dual emission with the maximum PL peaks at 545 nm and 730 nm (Fig. 2i). The green emission is originated from the $[Pb_3Br_{11}]^{5-}$ trimer, and $PbBr_4^{2-}$ tetrahedron is non-emissive similar to previous reported $(C_9NH_{20})_7(PbCl_4)Pb_3Cl_{11}$ system[38]. On the other hand, $SbBr_4^-$ tetrahedron is responsible from the emission at 730 nm, and the red shift from 670 to 730 nm is probably due to the tetrahedron transformation from the distorted seesaw shape into near regular tetrahedron. The PLE bands of green/red dual emission still remains separated with little overlap (Fig. 2e and Supplementary Fig. 15). When exciting fresh 395-K-annealed Pb-Br: Sb with different excitation wavelengths, various green/red dual emission profiles distinct $I_{730\ nm}/I_{545\ nm}$ values from 0.013 to 5 were characterized (Fig. 2i). Particularly, a warm white emission is obtained at 400 nm excitation while green and red emission present under 360 nm and 420 nm excitation (Fig. 2i (i-iii)). The excitation-wavelength-dependent CIE coordinates present a linear trajectory between green point (0.310, 0.556) and red point (0.464, 0.434), which have been detailed summarized in Supplementary Table 4.

Dual emisison mechanism of Pb-Br: Sb single crystal

In order to gain deeper insight into the STE dynamics in the excited energy levels, ultrafast PL emission process is recorded by the streak camera monitoring the picosecond time range. As shown in Fig. 3a, synchronous PL onset and decay curves at 470 and 670 nm were observed in Pb-Br: Sb, confirming the independent working mechanism between two emitters without mutual interaction. Moreover, femto-second transient absorption (fs-TA) spectra characterizations were further carried out. As shown in Fig. 3b and c, broad photo-induced absorption (PIA) covering the whole visible region were observed in Pb-Br: Sb, corresponding to the formation of additional excited-states in the below-gap region. The possible role of permanent defect states has been excluded from a linear dependence of PL intensities on excitation intensity, thus pointing to STE formation (Supplementary Fig. 16). Considering that the excited carrier density can be rationally interpreted by the ΔA intensity, PIA signal is dominated by high-energy region when pumping at 360 nm pulse, suggesting photo-generated STEs are mainly populated at $PbBr_4^{2-}$ clusters thus resulting in blue emission (Fig. 3b). Equally matched dual PIA bands appear at 450 nm and 650 nm when pumping at 390 nm, indicating uniformly-distributed STEs density in two emitters thus leading to white light emission (Fig. 3c). Different PL emission lifetimes were observed when probing at two emission band further confirmed the existence of two emitters (Supplementary Figs. 17, 18). By comparing the UV-vis light absorbance spectra between Pb-Br and Pb-Br: Sb, it can be found that Pb-Br is nearly inert to the photons with wavelength longer than 400 nm, while Sb^{3+}-associated species are relatively photoactive in this region, leading to bright red emission. On the other hand, $SbBr_4^-$ species are uncompetitive to harvesting the high energy photons probably due to the low doping amount, and thus in this case blue emission is predominant. Therefore, precise control of excitation wavelength could result in the dynamic STE distribution in these two independent emitting states, thus leading to dynamic color tunable luminescence.

To better illustrate the impact of Sb^{3+} dopant on the electronic properties of Pb-Br, density functional theory (DFT) calculation has been performed. In this case, it is proposed the deprotonation of 1-butyl-1-methyl-piperidinium forms together with $SbBr_4^-$ unit to keep the charge balance, similar to the previously reported Sb^{3+} doped $[NH_3(CH_2)_4NH_3]CdBr_4$ system[31]. As shown in Fig. 3d, the atomic-orbital density of states (DOS) of undoped Pb-Br reveal highest occupied molecular orbital (HOMO) and the lowest unoccupied molecular orbital (LUMO) are mainly dominated by $PbBr_4^{2-}$ clusters with little participation from organic cations. Negligible electronic interaction is formed between neighboring $PbBr_4^{2-}$ species, which suggests each $PbBr_4^{2-}$ cluster can act as an independent STE emitter in the 0D system (Fig. 3e and f). After introduction of Sb^{3+}, excited states near the LUMO appear and narrow down the bandgap as a result of the hybridization of Sb-5s/p and Br-4p orbitals (Fig. 3g), which further indicates $SbBr_4^-$ species could function as additional traps to capture low-energy excitons by photo-induced lattice distortion and generate efficient red STE emission. Additionally, the LUMO energy levels of $PbBr_4^{2-}$ and $SbBr_4^-$ units are highly split, proving non-mutual interactions between two STE excited states. Based on the above experimental results and calculated studies, the schematic diagrams of blue/red dual emissive phase I and green/red phase II are depicted in Fig. 4. Upon excitation, photo-generated exciton will be trapped into the seesaw shaped $PbBr_4^{2-}$ and $SbBr_4^-$ species as a result of the transient lattice deformation. During the de-excitation process to the ground states, blue/red dual emission centering at 470 nm and 670 nm is presented which can be assigned to the $^3P_1$ to $^1S_0$ transition. After thermal-induced transition, seesaw-structured $PbBr_4^{2-}$ and $SbBr_4^-$ units will transform into $[Pb_3Br_{11}]^{5-}$ trimer and $SbBr_4^-$ tetrahedra, which exhibit green and red STE emission peaking at 545 nm and 730 nm, respectively. Pb^{2+} and Sb^{3+}-associated STE emitter work independently in two phases, thus triggering double-model excitation-dependent color-tunable emission (Fig. 4b, c).

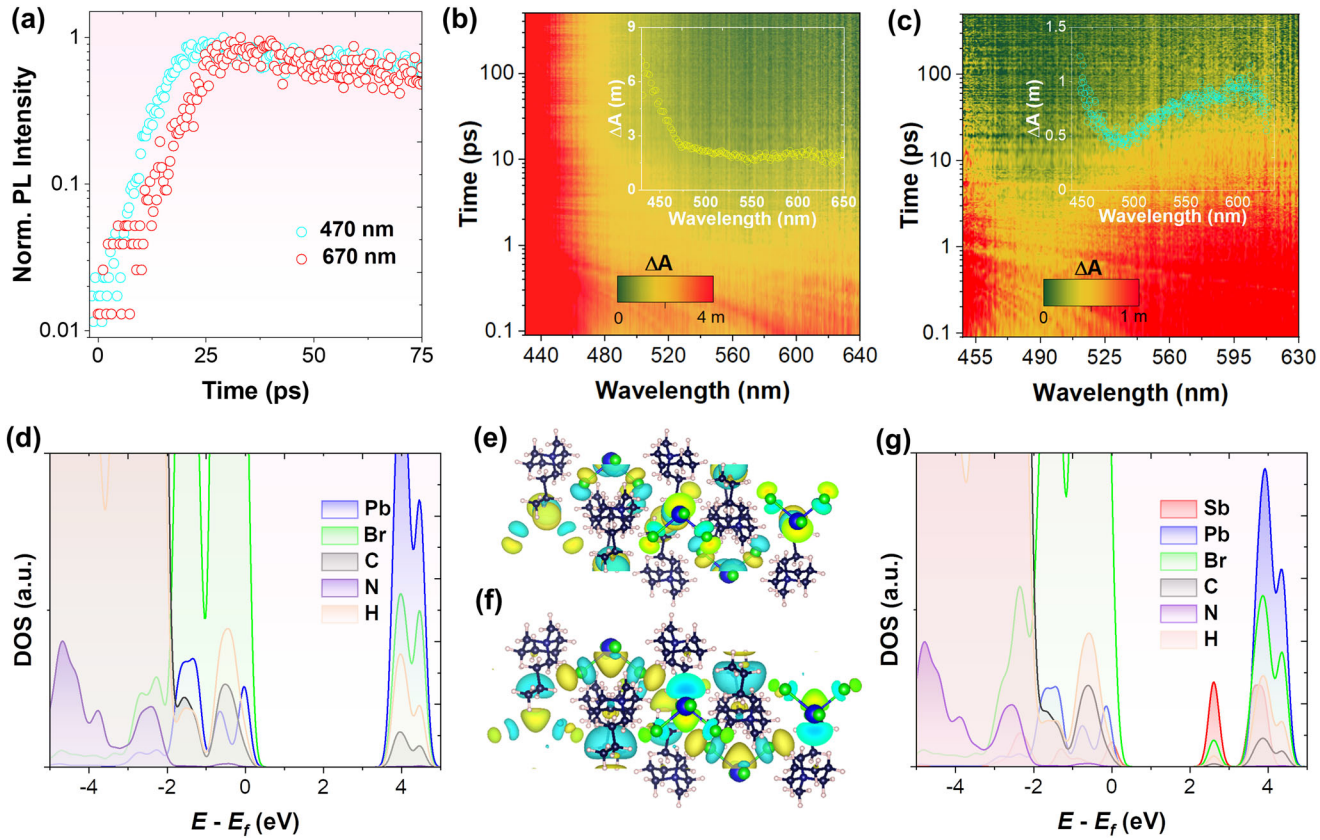

Fig. 3 Emission mechanism. a Time-resolved PL emission rise curves monitoring at two emission bands in Pb-Br: Sb. Pseudo-color fs-TA plot of Pb-Br: Sb pumping at 360 nm (**b**) and 390 nm (**c**) pulse, respectively. Inset shows the representative fs-TA spectra. Calculated atomic-orbital DOS of undoped (**d**) and Sb^{3+} doped (**g**) Pb-Br. Calculated HOMO (**e**) and LUMO (**f**) for the ground states of Pb-Br.

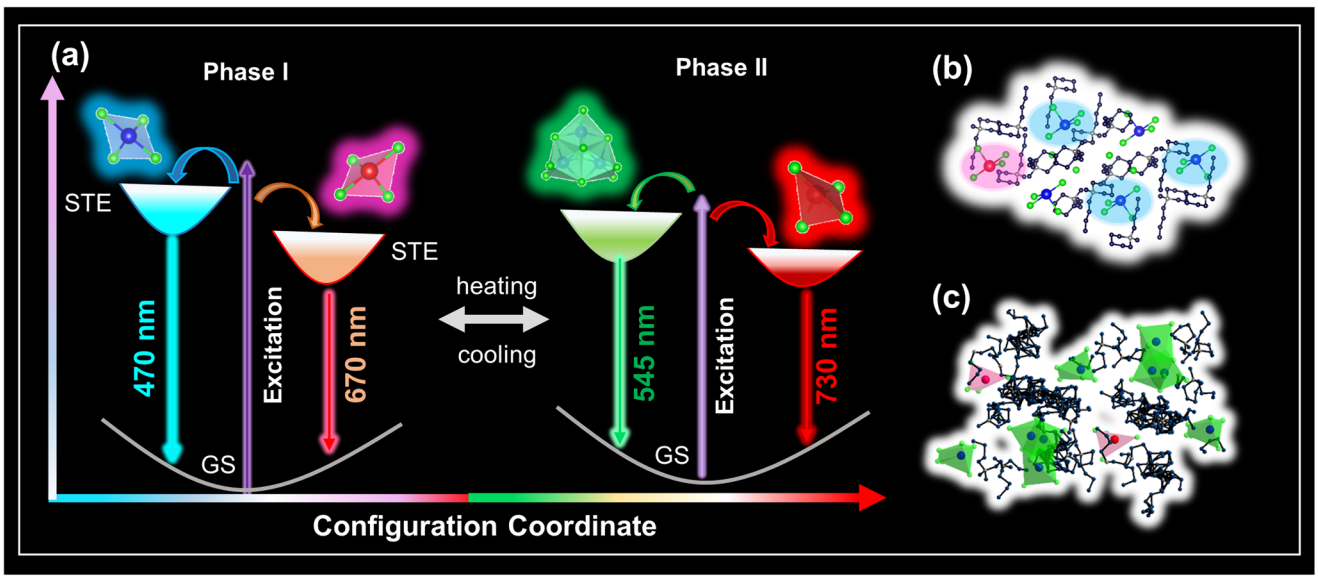

Fig. 4 Structure dependent emission properties. a Configuration diagrams of the phase-dependent dual emission processes in Pb-Br: Sb and the emission properties of different metal halide polyhedron units. Scheme view of (**b**) blue/red dual emissive Pb-Br: Sb (phase I) and (**c**) green-red dual emission after phase transformation (phase II).

Application of Pb-Br: Sb in anti-counterfeiting

The attractive red/green/blue/white widely-tunable emissive properties of Pb-Br: Sb under external stimulus (temperature and excitation wavelength) endow them with great potential in the fields of high-security anti-counterfeiting and encryption. More encouragingly, it is found Pb-Br: Sb phosphor powder could be prepared via a simple and convenient ultrasonic agitation method, which is beneficial for the large-scale production

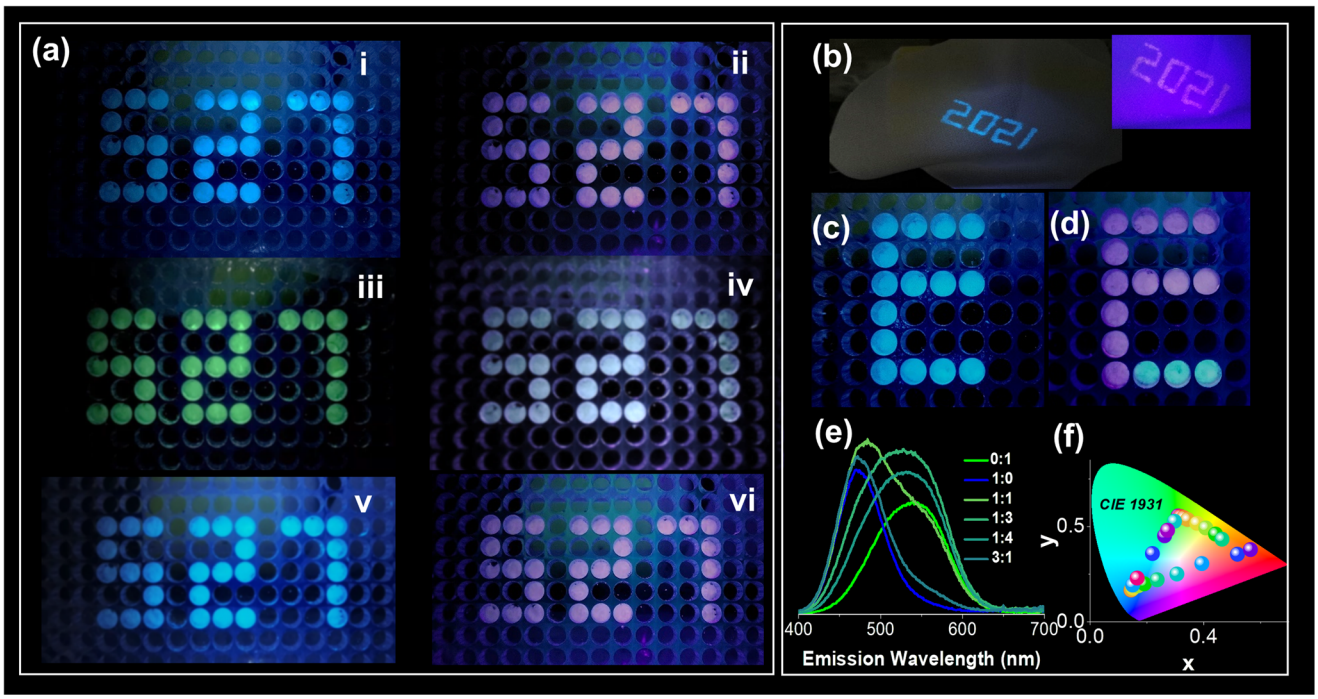

Fig. 5 Anti-counterfeiting and encryption application. a Optical images of Pb-Br: Sb powder encrypted "527" pattern under different circumstance: exciting at (i) 365 nm and (ii)395 nm UV light; heating at 110 °C and immediately excitation at (iii) 365 nm and (iv) 395 nm UV light; placing at ambient temperature for two days and excitation at (v) 365 nm and (vi) 395 nm UV light. **b** Optical images of wiper with hand-written "2021" under 365 nm UV light and 395 nm UV light. Pb-Br: Sb and Pb-Br powder encrypted pattern under (**c**) 365 nm and (**d**) 395 nm UV light. **e** PL emission spectra of the mixture of two phased Pb-Br: Sb with different weight ratios. **f** Summarized entire emission color of Pb-Br: Sb under different working models.

(Supplementary Fig. 19). As presented in Fig. 5a, a number pattern is encrypted by Pb-Br: Sb powder, which turns into blue "527" under 365 nm UV light and then changes to magenta color under the excitation at 395 nm (Fig. 5a (i, ii)). Upon heating at 110 °C for 2 min, the number "527" transformed into green and white light under 365 and 395 nm light excitation (Fig. 5a (iii, iv)). After stored in ambient air for two days, the "527" pattern could return back to the blue and magenta color (Fig. 5a (v, vi)). Furthermore, Pb-Br: Sb powder could be further prepared as a luminescent ink, based on which, information can be readily encrypted on flexible wiper. As shown Fig. 5b, digital code "2021" is handwritten with the Pb-Sb: Br ink, which appears with blue while magenta emission under 365 and 395 nm excitation, respectively. Figure 5c, d display a misleading pattern that are encrypted with Pb-Br and Pb-Br: Sb powder. Upon excitation at 365 nm, a blue "E" appears, while it evolves into a magenta "F" and a blue "_" under illumination at 395 nm UV light due to the chromatic luminescence switching of the Pb-Br: Sb. Additionally, it is found that the emission color could be tuned between blue and green by blending two phases Pb-Br: Sb (Fig. 5e). As demonstrated in Fig. S20, the corresponding CIE coordinates of phosphor mixture could be predictable and conveniently reproducible in the strict line, agreeing well with the additive color theory. As a result of the reversible phase transition, different weight ratioed phosphor mixture would return back to blue emission color (Supplementary Fig. 21). It is worth to note the phase transition from phase II to phase I is not sensitive to the temperature, and usually several days are required. Based on the above discussion, the entire emission color range of Pb-Br: Sb has been summarized in Fig. 5f, which can cover the RGB color triangle on the CIE 1931 diagram by rationally controlling the excitation wavelength and temperature (Supplementary Fig. 22).

DISCUSSION

In summary, we successfully developed a wide-range emission color-tunable lead halide single crystal based on Sb^{3+} doping and phase-transition strategy. The coexistence of extrinsic $SbBr_4^-$ and intrinsic $PbBr_4^{2-}$ STE emitters in a single phase enables a distinctive blue/red dual emission of Sb^{3+}-doped $(C_{10}NH_{22})_2PbBr_4$. The dual emission colors can be transformed to green/red after phase transition, which as far as we know is the first reported color-transformable dual-emissive metal halide materials. Due to the nonexistent mutual interaction, two emitters can be selectively or synchronously activated by controlling the excitation wavelengths, thus enabling a wide-range tunable emission color, including blue, green, red and white. Additionally, the tunable PL color and robust stability greatly expand the multifunctional applications of $(C_{10}NH_{22})_2PbBr_4$: Sb. This work not only presents an alternative design strategy towards full-color tunable emissive metal halide materials but also paves way for future exploration of advanced multifunctional phosphors by tailoring emitting units.

METHODS

Synthesis of undoped and Sb^{3+}-doped $(C_{10}NH_{22})_2PbBr_4$ single crystals

For the undoped single crystal, a clear mother solution was prepared firstly by dissolving a mixture of $PbBr_2$ (lead bromide, 0.4 mmol, 147 mg) and $(C_{10}NH_{22})Br$ ((1-butyl-1-methyl-piperidinium bromide), 0.8 mmol, 190 mg) in dimethylformamide (DMF). And then diethyl ether (Et_2O) vapor slowly diffuses into the mother solution at room temperature to crystallize the crystal. Same procedures were employed for the preparation of Sb^{3+}-doped $(C_{10}NH_{22})PbBr_4$ except that 5 mg of $SbBr_3$ (antimony bromide) was added in the precursor solution.

Synthesis of undoped and Sb^{3+}-doped $(C_{10}NH_{22})_2PbBr_4$ powder

A mixture of $PbBr_2$ (0.4 mmol, 147 mg), $SbBr_3$ (0.01 mmol, 5 mg) and $(C_{10}NH_{22})Br$ (0.8 mmol, 190 mg) was dispersed into a small amount of DMF before ultrasonic agitation for 60 s. The powders were collected by centrifugation and washed by Et_2O for three times before vacuum drying.

Characterizations

The optical micrograph of Pb-Br and Pb-Br: Sb was obtained using an inverted Nikon Ti epifluorescence microscope. Single crystal X-ray diffraction data of Pb-Br and Pb-Br: Sb were collected from Agilent Technologies Gemini A Ultra system with Cu-Kα radiation (λ = 1.54178 Å) at 150(10) K. Room temperature powder X-Ray Diffraction (PXRD) patterns were collected on X-ray diffractometer (SmartLab Rigaku, Japan) with Cu Kα radiation (λ = 1.5406 Å). Temperature-dependent PXRD patterns of Pb-Br were collected on a RIGAKU X-ray diffractometer (D-MAX 2200 VPC). X-ray photoelectron spectroscopy (XPS) were carried out on a Thermo-VG Scientific ESCALAB 250 X-ray photoelectron spectrometer. The scanning electron microscopy (SEM) morphological characterization and elemental mapping were obtained by high-resolution field emission scanning electron microscopy (SEM, Zeiss SIGMA, USA). Thermogravimetric analysis (TGA) was performed under N_2 environment using a NetzschTG209F3 TGA system with the samples heating from room temperature to 600 °C at a rate of 10 °C min^{-1}. Differential scanning calorimetry (DSC) was performed on a DSC 250 (TA Instruments) at a constant heating/cooling rate of 10 °C min^{-1} in nitrogen atmosphere. UV-vis absorption spectra of Pb-Br and Pb-Br: Sb powder were collected on an ultraviolet-visible spectrophotometer (V-770, Jasco, Japan). The room-temperature and low-temperature photoluminescence (PL) spectra were recorded by a fluorescence spectrophotometer (SP-2300, Princeton Instruments, USA). The power-dependent PL spectra were collected by a fiber-coupled spectrometer using a femtosecond-pulse laser (OPerA Solo, Coherent) as the excitation light with a range of neutral-density filters to adjust the power intensity. Femtosecond transient absorption spectra were measured on a Helios (Ultrafast Systems LLC) pump-probe setup. The pump pulse was generated in a collinear optical parametric amplifier (OPerA Solo, Coherent) pumped by 800 nm fundamental pulses (100 fs, 1 kHz repetition rate, Astrella-Tunable-V-F-1k, Coherent) and broad white light continuum probe light was generated from a sapphire crystal. Time-resolved PL emission spectra were recorded using a streak camera system (C10910, HAMAMATSU, Japan) and the laser source was the Coherent Legend regenerative amplifier (150 fs, 1 kHz, 800 nm) seeded by a Coherent Vitesse oscillator (100 fs, 80 MHz) (Helios, Germany). Density function theory calculation were performed by using the CP2K package. Perdew Burke-Ernzerhof (PBE) functional with Grimme D3 correction was used to describe the system. Unrestricted Kohn-Sham DFT has been used as the electronic structure method in the framework of the Gaussian and plane waves method. The Goedecker-Teter-Hutter (GTH) pseudo potentials, DZVP-MOLOPT-SR-GTH basis sets were utilized to describe the molecules. A plane-wave energy cut-off of 500 Ry has been employed, and the lattice parameters were fixed at the experimentally measured values while the atomic positions were optimized.

DATA AVAILABILITY

All relevant data that support the findings of this study are available from authors upon reasonable request.

Received: 24 February 2022; Accepted: 22 June 2022;
Published online: 11 July 2022

REFERENCES

1. Wu, W. Q. et al. Suppressing interfacial charge recombination in electron-transport-layer-free perovskite solar cells to give an efficiency exceeding 21%. *Angew. Chem. Int. Ed.* **132**, 21166–21173 (2020).
2. Zhang, Z. et al. Self-assembled lead-free double perovskite-MXene heterostructure with efficient charge separation for photocatalytic CO_2 reduction. *Appl. Catal. B* **312**, 121358 (2022).
3. Tsai, H. et al. Bright and stable light-emitting diodes made with perovskite nanocrystals stabilized in metal-organic frameworks. *Nat. Photonics* **15**, 843–849 (2021).
4. Li, Q. et al. Pressure-induced remarkable enhancement of self-Trapped exciton emission in one-dimensional $CsCu_2I_3$ with tetrahedral units. *J. Am. Chem. Soc.* **142**, 1786–1791 (2020).
5. Zhou, L. et al. Intrinsic self-trapped emission in 0D lead-free $(C_4H_{14}N_2)_2In_2Br_{10}$ single crystal. *Angew. Chem. Int. Ed.* **131**, 15581–15586 (2019).
6. Wei, J.-H. et al. Kuang, Indium-antimony-halide single crystals for high-efficiency white-light emission and anti-counterfeiting. *Sci. Adv.* **7**, eabg3989 (2021).
7. Han, Y., Yue, S. & Cui, B. B. Low-dimensional metal halide perovskite crystal materials: structure strategies and luminescence applications. *Adv. Sci.* **8**, 2004805 (2021).
8. Li, S., Luo, J., Liu, J. & Tang, J. Self-trapped excitons in all-inorganic halide perovskites: fundamentals, status, and potential applications. *J. Phys. Chem. Lett.* **10**, 1999–2007 (2019).
9. Mao, L., Wu, Y., Stoumpos, C. C., Wasielewski, M. R. & Kanatzidis, M. G. White-light emission and structural distortion in new corrugated two-dimensional lead bromide perovskites. *J. Am. Chem. Soc.* **139**, 5210–5215 (2017).
10. Yakunin, S. et al. High-resolution remote thermometry and thermography using luminescent low-dimensional tin-halide perovskites. *Nat. Mater.* **18**, 846–852 (2019).
11. Li, M. & Xia, Z. Recent progress of zero-dimensional luminescent metal halides. *Chem. Soc. Rev.* **50**, 2626–2662 (2021).
12. Wu, X., Trinh, M. T. & Zhu, X. Y. Excitonic many-body interactions in two-dimensional lead iodide perovskite quantum wells. *J. Phys. Chem. C.* **119**, 14714–14721 (2015).
13. Tan, Z. et al. Lead-free perovskite variant solid solutions $Cs_2Sn_{1-x}Te_xCl_6$: bright luminescence and high anti-water stability. *Adv. Mater.* **32**, 2002443 (2020).
14. Liu, F. et al. Light-emitting metal-organic halide 1D and 2D structures: near-unity quantum efficiency, low-loss optical waveguide and highly polarized emission. *Angew. Chem. Int. Ed.* **133**, 13548–13553 (2021).
15. Jun, T. et al. Lead-free highly efficient blue-emitting $Cs_3Cu_2I_5$ with 0D electronic structure. *Adv. Mater.* **30**, 1804547 (2018).
16. Zhou, C. et al. Luminescent zero-dimensional organic metal halide hybrids with near-unity quantum efficiency. *Chem. Sci.* **9**, 586–593 (2018).
17. Zhou, L., Liao, J. F. & Kuang, D. B. An overview for zero-dimensional broadband emissive metal-halide single crystals. *Adv. Optical Mater.* **9**, 2100544 (2021).
18. Zhou, C. et al. Highly efficient broadband yellow phosphor based on zero-dimensional tin mixed-halide perovskite. *ACS Appl. Mater. Interfaces* **9**, 44579–44583 (2017).
19. Zavaleta, A. et al. Full visible spectrum and white light emission with a single, input-tunable organic fluorophore. *J. Am. Chem. Soc.* **142**, 20306–20312 (2020).
20. Peng, H. et al. Bulk assembly of a 0D organic antimony chloride hybrid with highly efficient orange dual emission by self-trapped states. *J. Mater. Chem. C.* **9**, 12184–12190 (2021).
21. Liu, Y. et al. Efficient, stable, and tunable cold/warm white light from lead-free halide double perovskites $Cs_2Zr_{1-x}Te_xCl_6$. *Adv. Optical Mater.* **9**, 2100815 (2021).
22. Chen, X. et al. Combination of two colorless fluorophores for full-color red-green-blue luminescence. *ACS Appl. Mater. Interfaces* **13**, 38629–38636 (2021).
23. Zhou, C. et al. Bulk assembly of multicomponent zero-dimensional metal halides with dual emission. *ACS Mater. Lett.* **2**, 376–380 (2020).
24. Liao, J. F. et al. Emission-color-tunable Pb-Sn alloyed single crystals with high luminescent efficiency and stability. *Adv. Optical Mater.* **10**, 2102426 (2022).
25. Xu, L. J. et al. Multicomponent organic metal halide hybrid with white emissions. *Angew. Chem. Int. Ed.* **132**, 14224–14227 (2020).
26. Li, M., Molokeev, M. S., Zhao, J. & Xia, Z. Optical functional units in zero-dimensional metal halides as a paradigm of tunable photoluminescence and multicomponent chromophores. *Adv. Optical Mater.* **8**, 1902114 (2020).
27. Chen, B. et al. Multiexcitonic emission in zero-dimensional Cs_2ZrCl_6:Sb^{3+} perovskite crystals. *J. Am. Chem. Soc.* **143**, 17599–17606 (2021).
28. Kong, Q. et al. Phase engineering of cesium manganese bromides nanocrystals with color-tunable emission. *Angew. Chem. Int. Ed.* **60**, 19653–19659 (2021).
29. Chang, T. et al. Efficient energy transfer in Te^{4+}-doped Cs_2ZrCl_6 vacancy-ordered perovskites and ultrahigh moisture stability via A-site Rb-alloying strategy. *J. Phys. Chem. Lett.* **12**, 1829–1837 (2021).
30. Zhou, J. et al. Tunable photoluminescence in Sb^{3+}-doped zero-dimensional hybrid metal halides with intrinsic and extrinsic self-trapped excitons. *J. Mater. Chem. C.* **8**, 5058–5063 (2020).
31. Wu, J. et al. Ultrafast study of exciton transfer in Sb (III)-doped two-dimensional $[NH_3(CH_2)_4NH_3]CdBr_4$ perovskite. *ACS Nano* **15**, 15354–15361 (2021).
32. Su, B., Li, M., Song, E. & Xia, Z. Sb^{3+}-doping in cesium zinc halides single crystals enabling high-efficiency near-infrared emission. *Adv. Funct. Mater.* **31**, 2105316 (2021).
33. Zhou, L. et al. Defect passivation in air-stable tin(IV)-halide single crystal for emissive self-trapped excitons. *Adv. Funct. Mater.* **31**, 2108561 (2021).
34. Morad, V. et al. Hybrid 0D antimony halides as air-stable luminophores for high-spatial-resolution remote thermography. *Adv. Mater.* **33**, 2007355 (2021).

35. Morad, V. et al. Disphenoidal zero-dimensional lead, tin, and germanium halides: highly emissive singlet and triplet self-trapped excitons and X-ray scintillation. *J. Am. Chem. Soc.* **141**, 9764–9768 (2019).
36. Fan, L. et al. Efficiency-tunable single-component white-light emission realized in hybrid halides through metal co-occupation. *ACS Appl. Mater. Interfaces* **13**, 29835–29842 (2021).
37. Gong, L. et al. Multimode dynamic luminescent switching of lead halide hybrids for anti-counterfeiting and encryption. *Chem. Eng. J.* **424**, 130544 (2020).
38. Zhou, C. et al. Blue emitting single crystalline assembly of metal halide clusters. *J. Am. Chem. Soc.* **140**, 13181–13184 (2018).

ACKNOWLEDGEMENTS

This work was supported by the Science and Technology Development Fund, Macao SAR (File no. FDCT-0044/2020/A1, 0082/2021/A2), UM's research fund (File no. MYRG2018-00148-IAPME, MYRG2020-00151-IAPME, MYRG2018-00142-IAPME), the Natural Science Foundation of China (61935017, 62175268), Natural Science Foundation of Guangdong Province, China (2019A1515012186), Guangdong-Hong Kong-Macao Joint Laboratory of Optoelectronic and Magnetic Functional Materials (2019B121205002), and Shenzhen-Hong Kong-Macao Science and Technology Innovation Project (Category C) (SGDX2020110309360100).

AUTHOR CONTRIBUTIONS

J.-F.L. and Z.Z. contributed equally to this work. J.F.L. conceived the idea and designed the experiments. G.C.X. and Z.K.T. supervised the work. J.F.L. prepared the single crystals. J.F.L. and Z.P.Z. contribute to the material structure characterizations and the optical studies. B.Z.W. carried out the fs-TA test. J.F.L. wrote the manuscript and Z.P.Z. and G.C.X. provided major revisions. All authors discussed the results and commented on the manuscript.

COMPETING INTERESTS

The authors declare no competing interests.

ADDITIONAL INFORMATION

Supplementary information The online version contains supplementary material available at https://doi.org/10.1038/s41528-022-00194-4.

Correspondence and requests for materials should be addressed to Zikang Tang or Guichuan Xing.